Supporting Information for "Large scale InSAR monitoring of permafrost freeze-thaw cycles on the Tibetan Plateau"

Simon Daout[1], Marie-Pierre Doin[1], Gilles Peltzer[2,3], Anne Socquet[1], Cécile Lasserre[1]

[1]ISTerre, Université Grenoble-Alpes, CNRS, Grenoble,

[2]Department of Earth Science, University of California, LA, USA

[3]Jet Propulsion Laboratory, California Institute of Technology, CA

1 Methods

This method section provides additional text and figures explaining and illustrating all the processing steps of the SAR data. We take as example the Envisat track 119, but applied the same processing scheme for all tracks. The purpose of this section is to optimize the retrieval of the permafrost signal within the interferograms and to provide a method for systematic InSAR processing in permafrost area.

Interferogram network: For the four tracks we first define an optimal small baseline interferometric network connecting with redundancy all acquisitions using perpendicular baseline constraint, B_{perp}, and temporal baseline constraint, B_t (Fig. S1). Note that some interferograms present either large B_{perp} and low B_t or low B_{perp} and large B_t. We then average all interferograms at 2 and 10 looks in the range and azimutal directions, respectively. Number of images and interferograms we used for each track are summarized in Table S1 and (Fig. S2). Except for track 348, all pixels are covered by more than 30 images.

Corrections before phase unwrapping: The processing is based on a series of corrections before unwrapping that reduces the variance of the wrapped phase. Fig. S3 presents an example of a long temporal baseline wrapped interferogram on track 119 before and after this series of corrections, which includes the stratified atmospheric delay correction using global atmospheric re-analysis model, ERA-Interim [*Doin et al.*, 2009; *Jolivet et al.*, 2011, 2014] (computed by the European Center for Medium-Range Weather Forecast (ECMWF)), the linear term correction in the range direction to correct for residual orbital errors, and local Digital Elevation Model (DEM) error correction. DEM errors

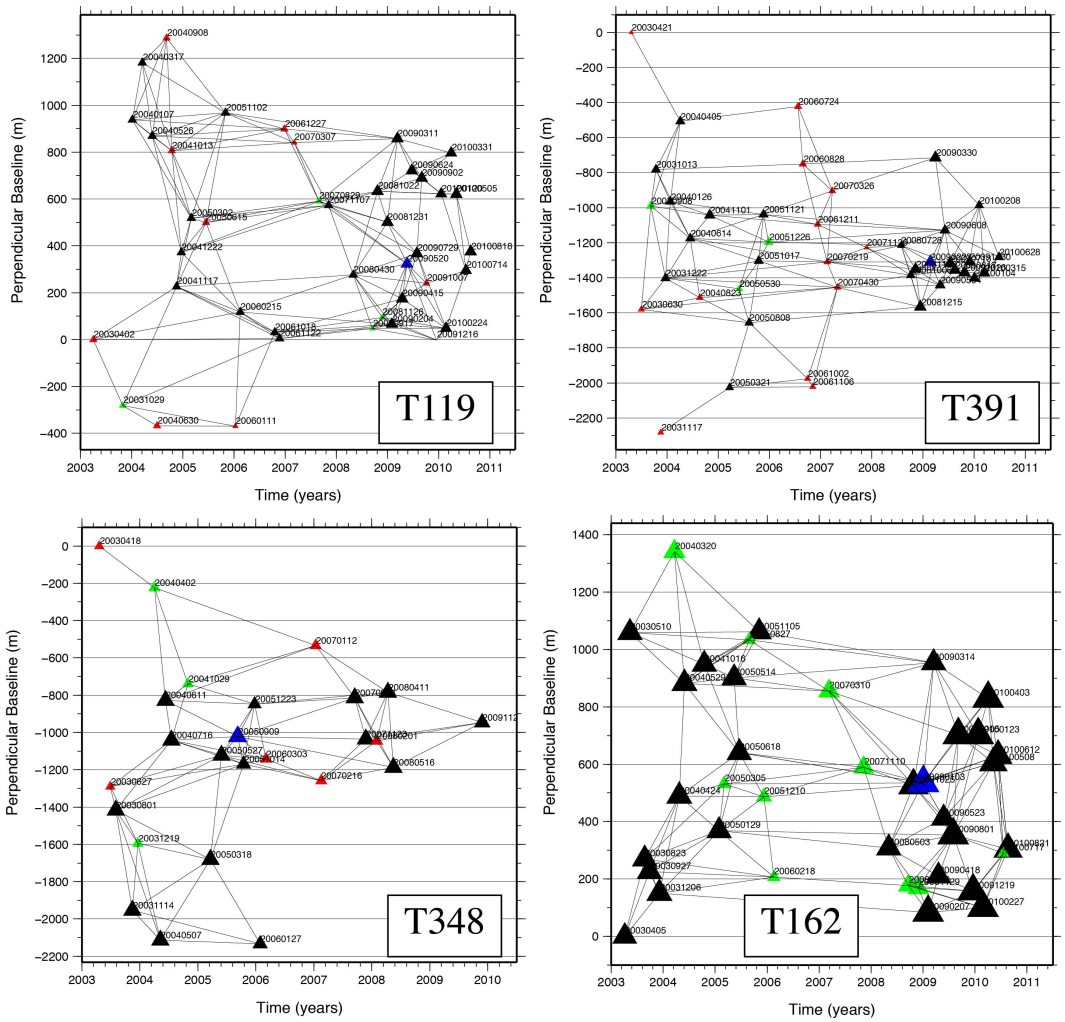

Figure S1. Computed interferograms for the four tracks. Triangles are SAR acquisitions with sizes and colors according to their spatial extent: black triangles for a full coverage, green triangles for images covering the northern part of the track only, and red colors for images covering the southern part only. The master image is shown with a blue triangle.

are after estimated based on the relationship between interferometric phase and perpendicular baseline [*Ducret et al.*, 2014].

ERA-I provides estimates of temperature, water vapor partial pressure, and geopotential height every six hours at different pressure levels on a 0.7° grid from 1989 to present [*Dee et al.*, 2011]. Path delays at each acquisition time are derived from vertical profiles of these variables at several ERA-I points encompassing a SAR scene. The delay is then mapped on the radar scene by integration for each pixel from a Digital Elevation Model (DEM) to the satellite elevation [*Doin et al.*, 2009]. To quantify the amplitude of this tro-

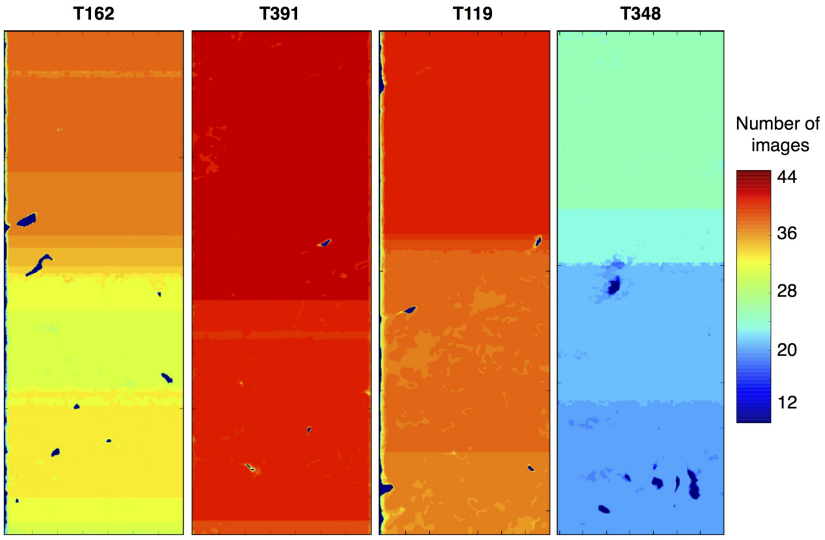

Figure S2. Number of images per pixel for the 4 tracks.

pospheric signal within the Tibetan plateau, we plot the relative delay between the valleys (4800 m) and the mountain ranges (5400 m) for one ERA-I point located in the Tibetan plateau (36°, 85.5°) (Fig. S4). The integrated path delays between the two elevations are computed relatively to the first date as function of time since each new year to better visualize the seasonal pattern (Fig. S4). The prediction indicates a slight seasonal pattern, peacking at the beginning of February, and a variability of 3.1 mm, smaller than the permafrost related signal. We correct interferograms from this predicted stratified atmospheric phase screen. Note that within the Tibetan plateau, we cannot compute for validation the residual phase-elevation correlation after ERA-I correction as the phase-elevation correlation is difficult to separate from permafrost signal in the valleys. Note also that this correction does not correct non-stratified patterns with wavelength lower than 75 km. However, the effect of turbulent patterns, being random both in space and time, are attenuated by data stacking in the following time series analysis.

Unwrapping procedure: To help the unwrapping, we implement a specific iterative procedure that consists in using a spatial template for deformation. This approach is standard in InSAR processing and has already been applied for land subsidence [e.g., *Strozzi and Wegmuller*, 1999; *López-Quiroz et al.*, 2009] or volcanic studies [e.g., *Yun et al.*, 2007; *Pinel et al.*, 2008] in presence of complex and large deformation. We here extract the template from a Principal Component Analysis (PCA) decomposition. We produce a first se-

Table S1. Table summarizing the number of images and interferograms per track.

Tracks	# of Images	# of Interferograms
T348	41	146
T119	25	75
T162	44	132
T162	38	142
Total	148	495

ries of unwrapped interferograms and check their reliability computing the misclosure of the interferometric network. We then perform the PCA from a selection of successfully unwrapped interferograms (presenting a low misclosure), $C = \mathcal{U} * \lambda * \mathcal{V}$, where $\mathcal{U}$ is the eigenvector matrix of the covariance matrix, C, between interferograms centered around the zero phase, λ, is the eigenvalue matrix, and $\mathcal{V}$, is the transformation matrix from the interferograms basis to the principal component basis. C is computed using only unwrapped pixels. Note that as the no data mask is slightly different from one interferograms to the other, C is not perfectly positive definite. The deformation pattern we are interested in pops up in the first or second component (Fig. S5a). Temporal inversion of the corresponding eigenvector shows, as expected, a seasonal signal.

The comparison of the deformation pattern extracted from PCA with elevation and google earth imagery shows that deformation is concentrated in basins and that "basement" can be considered, on average, as non deforming. We must thus insure that the deformation template extracted from PCA map is on average referenced to zero on basement. To do so, we extract a N-S profile (Fig. S5b) and observe that PCA values on basement pixels have far less scatter than the PCA values on basin pixels. To define a N-S reference curve, we fit across the median of pixels selected in areas with less scatter (red median) a cubic ramp in azimuth (blue line in Fig. S5b). This ramp in azimuth is removed from the PCA as shown in Fig. S5c.

We repeat the operation for the four tracks and observe a good spatial continuity of the extracted deformation shape on the overlapping areas that correlates with the low elevation basins (Fig. S6).

Then, following *López-Quiroz et al.* [2009], we use the PCA map as a deformation template to help unwrapping in high fringe rate areas. We estimate a best-fit scaling co-

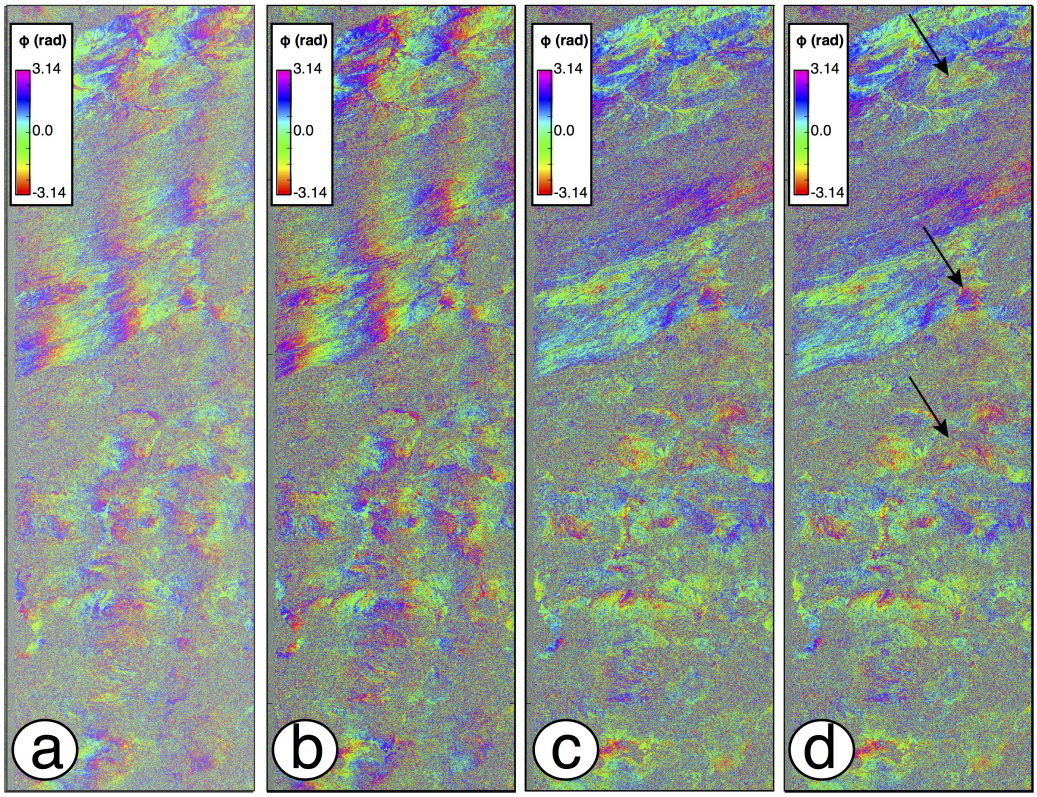

Figure S3. Example of corrections on the wrapped phase for a small B_{perp} of 50 m and long temporal baseline interferogram between the two images acquired in November 17, 2004 and April 30, 2008 for track 119. a) Original interferogram in 4x20 looks. b) Interferogram after ERAI correction. c) Interferogram after range ramp correction. d) Interferogram after local DEM errors correction. (a), (b) and (c) are superimposed to the coherence, while (d) is superimposed to the phase colinearity. Arrows point out some areas with strong phase discontinuities.

efficient between the deformation template and the wrapped phase (by maximizing the complex coherence of the residue), and remove the scaled template from the original interferogram (Fig. S7, Fig. S8). Before corrections (Fig. S7a,b), black arrows point out typical patterns of deformation dominating the wrapped phase. After correction, these patterns are in majority removed (Fig. S7c) and the phase is more easily unwrapped (Fig. S7d).

In addition to this iterative procedure, unwrapping process is performed using a specific scheme. First, we multilook by a factor of 8 in range and 40 in azimuth, replacing the amplitude of the interferograms by the colinearity as defined by *Pinel-Puyssegur et al.* [2012] (Fig. S7a). We then low pass filter using the average temporal coherence as weight (Fig. S7b). In contrast to the cut-tree algorithm [*Rosen et al.*, 2004], here we impose an

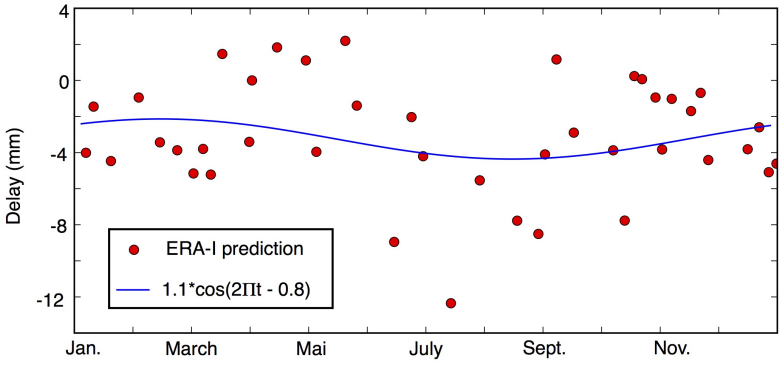

Figure S4. Time series of the predicted tropospheric delay for a ERA-I point located within the Tibetan plateau (36°, 85.5°) between elevations of 4800 m and 5400 m. The standard deviation of the stratified atmospheric signal predicted by ERA-I is 3 mm, which is smaller than the permafrost related signal, and with slight seasonal pattern picking at the beginning of February.

unwrapping path going from the high to low coherence areas defined by the filter, avoiding unwrapping to propagate into incoherent areas, as snow-capped mountain ridges or across areas of very high rate. Unwrapping is performed in adjoining sub-regions above a coherence threshold. Each newly unwrapped area is added to already unwrapped areas. The coherence threshold progressively decreases to propagate unwrapping further away [*Grandin et al.*, 2012; *Doin et al.*, 2015; *Daout et al.*, 2016]. If necessary, high priority bridges are set manually by visual inspection of interferograms.

We finally reintroduce the scaled template previously removed (Fig. S7e). Note that if the computed template was not in agreement with the interferograms, the scaling factor between both would tend to be zero. This would lead to a small but inappropriate correction of wrapped interferograms and an increasing of the unwrapping errors. We checked this by computing the misclosure of the unwrapped interferogram network at each iterations, which remain small for most pixels (< 0.5 rad). Doing so, we successfully produce wide, continuous and high quality unwrapped interferograms covering the northwestern part of the Tibetan plateau.

Fig. S8 shows three examples of wrapped and unfiltered interferograms presenting strong permafrost related deformation. Before corrections (Fig. S8a), black arrows

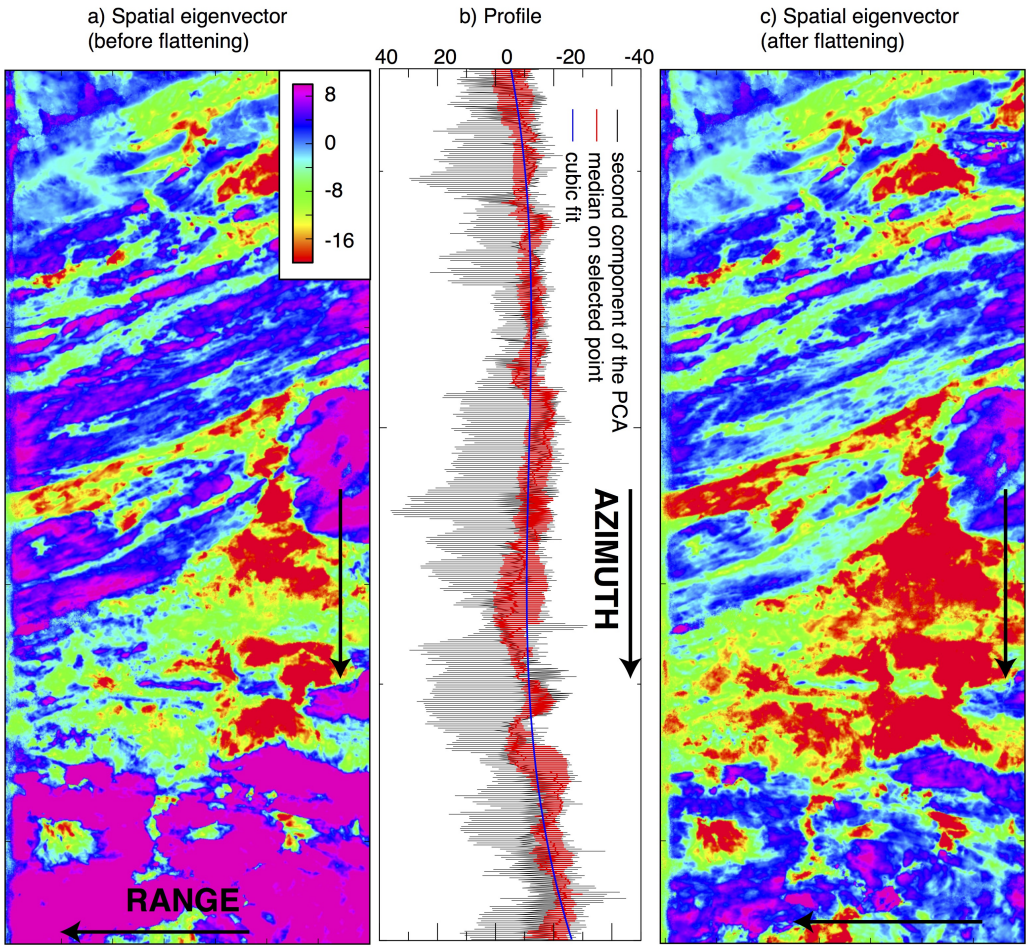

Figure S5. Second component of the PCA decomposition for track 119. a) Spatial eigenvector. b) Eigenvector profile (black lines). The bedrock is characterized by relatively more positive values than the basins that show more scatter. Cubic ramp (blue line) estimated from the median computed on selected points on "bedrock" (red line). c) Spatial eigenvector after flattening from the cubic ramp to reference at zero on basement.

point out typical patterns of deformations dominating the wrapped phase. After correction (Fig. S8b), these patterns are in majority removed and the phase is easily unwrapped.

Time series analysis: At the end of the processing, interferograms are inverted into successive phase delays maps (Fig. S9a). This step is crucial as it allows to check the consistency of each interferogram and thus detect the residual unwrapping errors [*López-Quiroz et al.*, 2009; *Doin et al.*, 2011]. Misclosure of the interferometric network are computed for each interferogram. If large, we then check visually the corresponding interferogram and correct its unwrapping errors. Times series analysis is then iterated again until

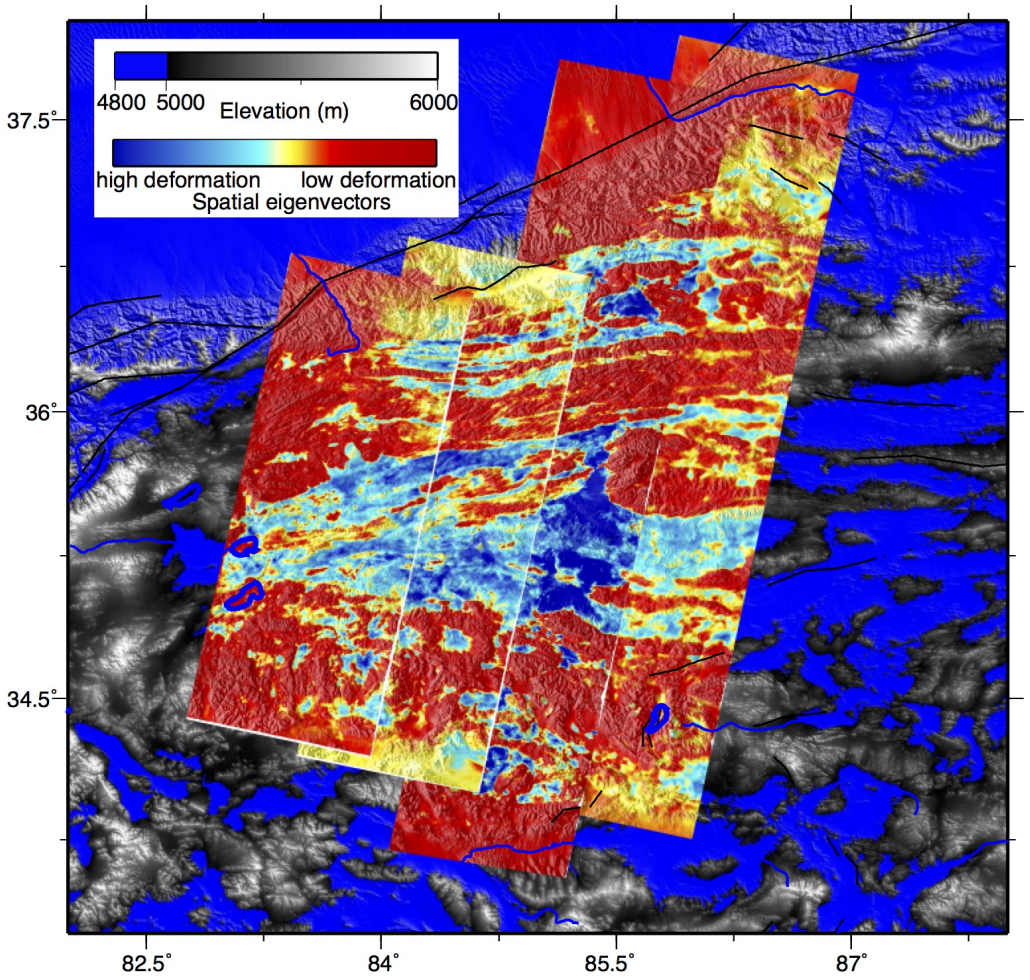

Figure S6. Spatial eigenvectors associated to the PCA component that presents a strong seasonality. Blue patterns are deforming areas while red colors highlight stable areas. These maps are used as templates to unwrap interferograms.

no large network inconsistencies remain [*Doin et al.*, 2015]. To refer the maps to a stable bedrock, we first mask the deformation areas using a threshold on the previous deformation shape extracted from the PCA (Fig. S6), and estimate a cubic ramp in azimuth and a quadratic ramp in range on bedrock areas for each phase delays maps to remove possible tectonic signal (that could be of the order of a few mm/yr in the LOS). So no single reference points are used but we set on average regional reference on non deforming pixels (Fig. S10). After correction of this large scale reference surface, we derive a linear term, V, a DEM error coefficient, α, a cosinus term, β_2, and a sinus term, β_1, such as:

$$\phi^k = \mathrm{V}t_k + \alpha B_\perp^k + \beta_1 * \sin wt_k + \beta_2 * \cos wt_k . \quad (1)$$

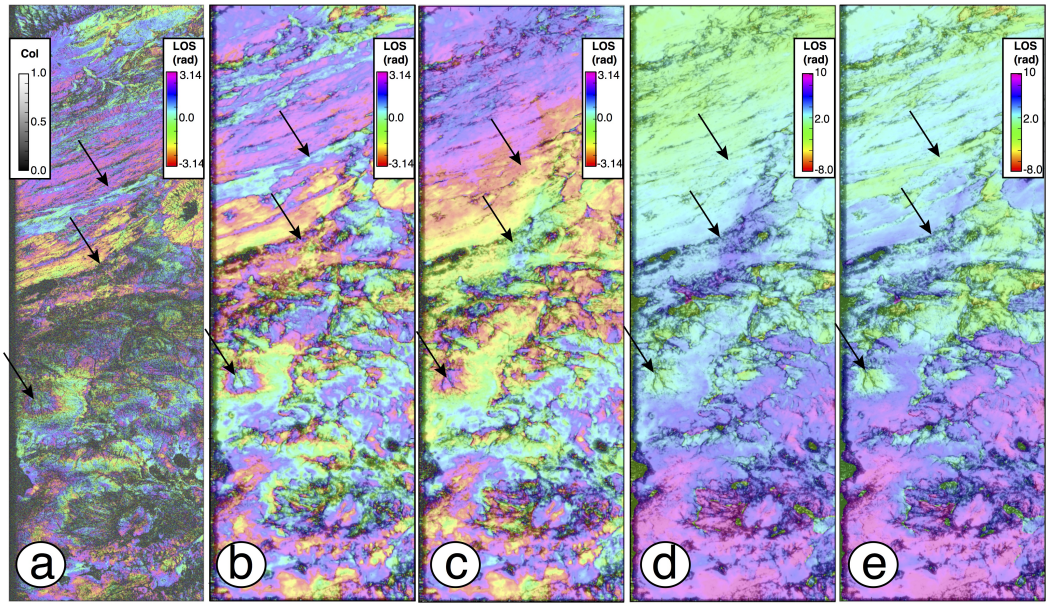

Figure S7. Example of unwrapping procedure for an interferogram of track 119. The interferogram is formed between the two images acquired on November 11, 2007 and April 30, 2008, for the track 119. Arrows highlight some examples of areas with strong phase discontinuities, where our procedure succeeds in unwrapping the pahse. a) Interferogram in 8x40 looks superimposed to the phase colinearity [*Pinel-Puyssegur et al.*, 2012]. b) Filtered interferogram superimposed to the coherence associated to the filter averaging process. c) Interferogram corrected using the PCA deformation template. d) Unwrapped interferogram. e) Unwrapped interferograms after re introducing the scaled PCA shape.

We solve the inverse problem, $\mathbf{d} = \mathbf{Gm}$, where $\mathbf{d}$ is the data vector made of the phase displacements, and $\mathbf{m}$ is the vector of model, with the least square solution and then produce amplitude ($\sqrt{\beta_1^2 + \beta_2^2}$), temporal lag (arctan $\frac{\beta_1}{\beta_2}$) and ground velocity (V) deformation maps. Model and residual maps are also shown in Fig. S9b,c. Note that here no temporal smoothing have been applied to ϕ^k. We also compute, for each pixel i and for each parameter j, an error, $\sigma_m^{i,j}$, equal to:

$$\sigma_{\mathbf{m}}^{i,j} = \sqrt{\frac{N}{N-M}(\sigma_{\mathbf{d}}^i)^2(\mathbf{G}^{\mathrm{T}}\mathbf{G})_j^{-1}}, \tag{2}$$

where N is the number of data, M the number of parameter, $(\sigma_d^i)^2$ is the RMS phase residual for each pixel j, and $(\mathbf{G}^{\mathrm{T}}\mathbf{G})_j^{-1}$ is the diagonal j, and then produce amplitude ($\sqrt{\sigma_{\beta_1}^2 + \sigma_{\beta_2}^2}$), temporal lag ($\frac{\sigma_{\beta_1}|\beta_2| + \sigma_{\beta_2}|\beta_1|}{\sigma_{\beta_1}^2 + \sigma_{\beta_2}^2}$) and ground velocity ($\sigma_{\mathrm{V}}$) error maps (Fig. S11). Computed errors are clearly lower than the measured deformation, with higher errors for track 348 that contains less images (Fig. S2).

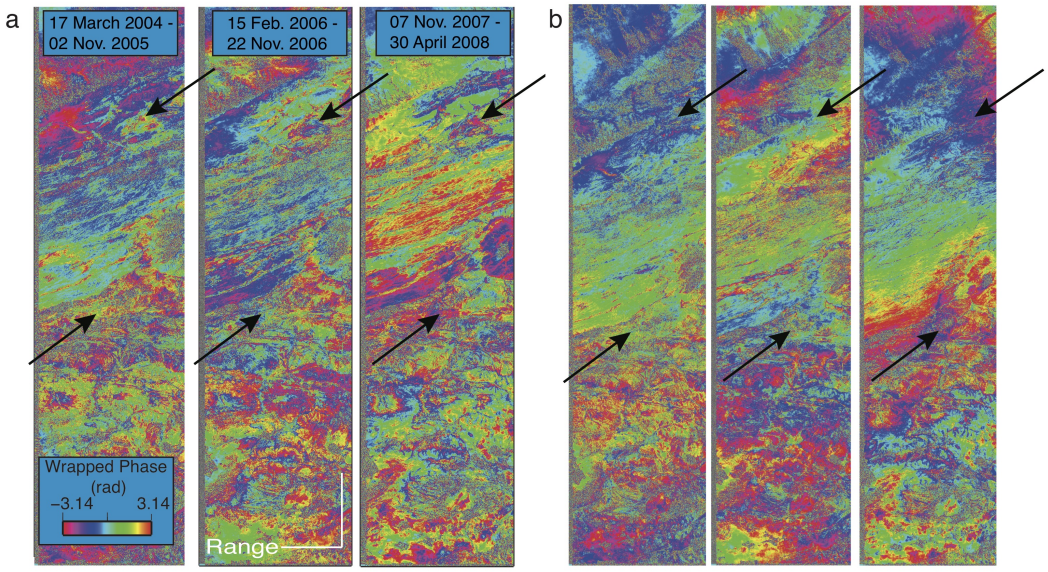

Figure S8. Example of three unfiltered interferograms on track 119. a) Wrapped interferograms after the series of correction explained in Fig. S3. b) Unwrapped interferograms from which PCA template of Fig. S5c has been removed to reduce locally the phase gradient and facilitate unwrapping.

2 Data Analysis

Comparisons: To characterize the spatial patterns of the observed signal, we superimpose its amplitude for track 119 on elevation, topography ruggedness, geological map and google earth imagery (Fig. S12). The deformation correlates with areas of low topography (Fig. S12a) and even more strikingly of low ruggedness (Fig. S12b). We observe an almost perfect match between the boundaries of the deforming area and those of the Cenozoic sediments (Fig. S12c), made from fine silt to coarser gravel sediments and conglomerates [*Pan et al.*, 2004]. Superimposition of amplitude on the Google Earth imagery similarly suggests that deformation is restricted to sedimentary basins (Fig. S12d).

For a more detailed comparison of the observed signal with the surface morphology of the area we provide maps of seasonal deformation, its time lag, and multi-annual subsidence or uplift rates attached to this Supplement Information document and openable in Google Earth (.kml and .png files).

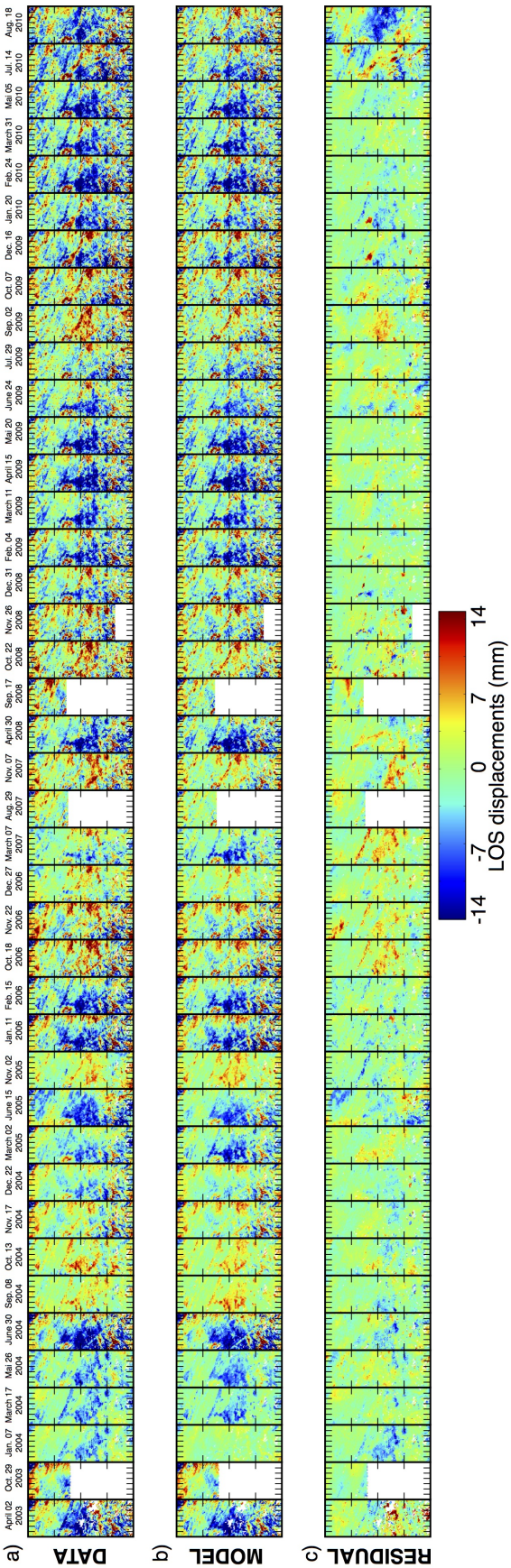

Figure S9. Time series of delay maps (a), models (b) and residuals (c) for track 119. One color cycle correspond to a LOS delay of 2.8 cm.

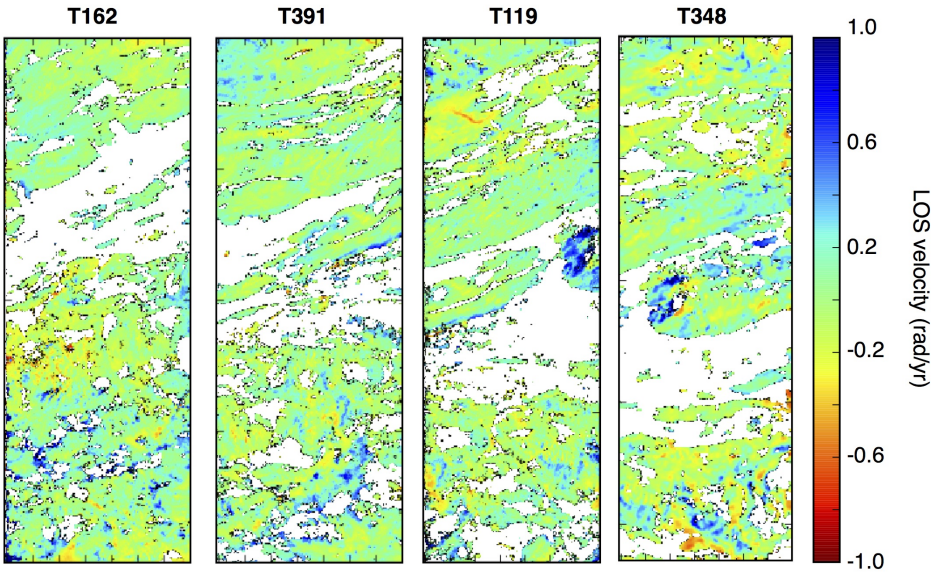

Figure S10. Long-term ground velocity of the defined bedrock for the 4 tracks after referencing.

Stefan model: The Stefan deformation model $m(t)$ [*Stefan*, 1891; *Leppäranta*, 1993] of Fig. 3B is defined as follow:

$$m(t_c < t < t_1) = c, \tag{3}$$

$$m(t_1 < t < t_2) = A_t * \sqrt{DDT(t)} + c, \tag{4}$$

$$m(t_2 < t < t_c) = -A_f * \sqrt{DDF(t)} + A_t * \sqrt{DDT(t_2)} + c, \tag{5}$$

where A_t and A_f are the thawing and freezing coefficients, respectively, $DDT(t)$ and $DDF(t)$ are the cumulative degree-day of thawing and freezing (time integrals of the ground temperature above or below zero), respectively, t_1, t_2, and t_c define the beginning of the thawing period, the beginning of the freezing period and the end of the freezing period, respectively, and c is a constant. Note that the SNR in the normalized curve of movements >8 mm is larger than that of the curve of movements <8 mm (Fig. 3B).

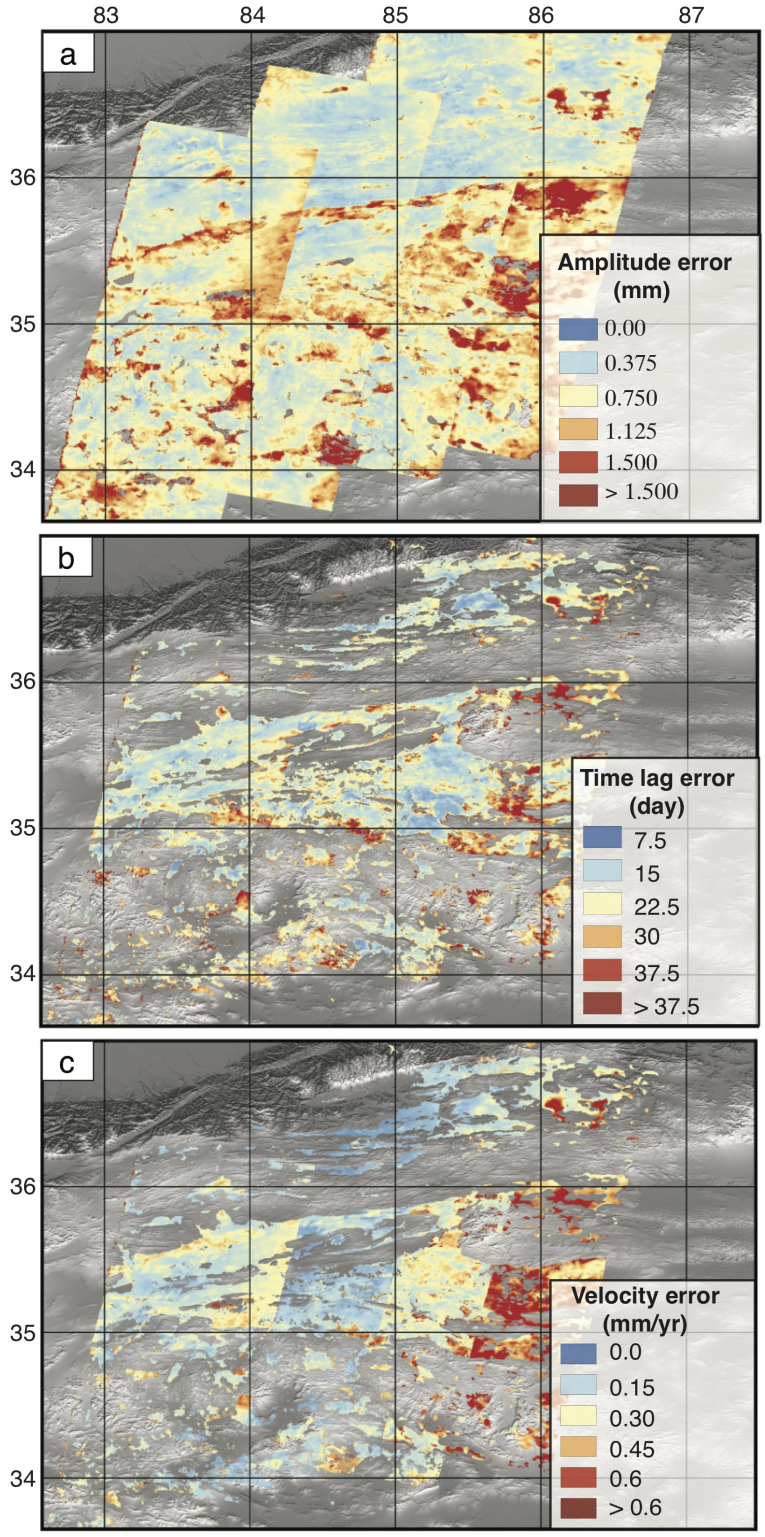

Figure S11. Errors maps for the parameters of the equation 2. a: Amplitude of the seasonal deformation. b: Time lag of peak subsidence. c: Multi-annual ground velocity.

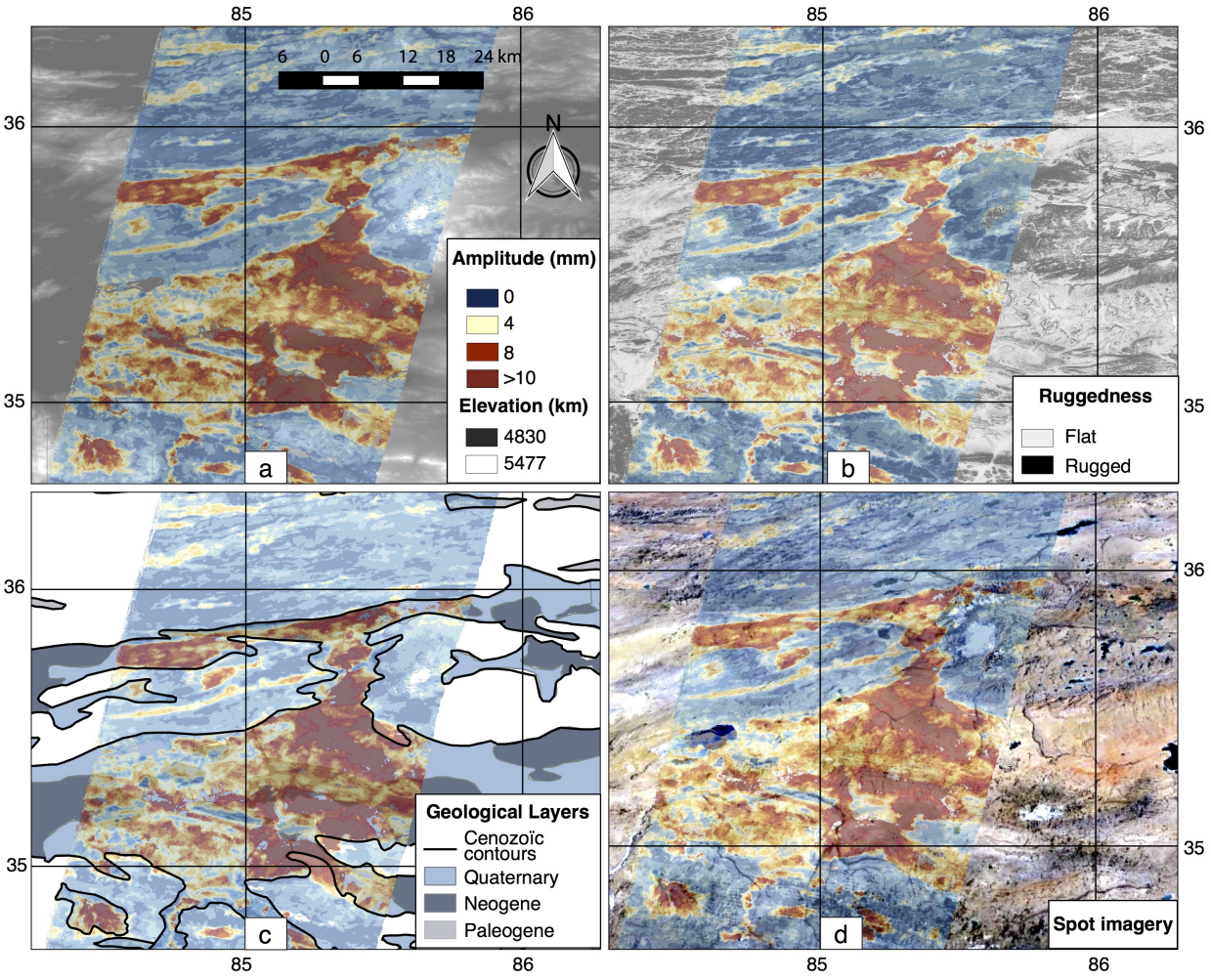

Figure S12. Zoom on the amplitude of the seasonal deformation for track 119 superimposed on DEM SRTM (a), on topography ruggedness index (b), on the geological map [*Pan et al.*, 2004] (c), and on CNES/Spot imagery from Google Earth (d).

References

Daout, S., R. Jolivet, C. Lasserre, M.-P. Doin, S. Barbot, P. Tapponnier, G. Peltzer, A. Socquet, and J. Sun (2016), Along-strike variations of the partitioning of convergence across the Haiyuan fault system detected by InSAR, *Geophys J. Int.*, *205*(1), 536–547.

Dee, D., S. Uppala, A. Simmons, P. Berrisford, P. Poli, S. Kobayashi, U. Andrae, M. Balmaseda, G. Balsamo, P. Bauer, et al. (2011), The ERA-Interim reanalysis: Configuration and performance of the data assimilation system, *Quarterly J. the Royal Meteorological Society*, *137*(656), 553–597.

Doin, M.-P., C. Lasserre, G. Peltzer, O. Cavalié, and C. Doubre (2009), Corrections of stratified tropospheric delays in SAR interferometriy: Validation with global atmospheric models, *J. Applied Geophysics*, *69*, 35–50.

Doin, M.-P., F. Lodge, S. Guillaso, R. Jolvet, C. Lasserre, G. Ducret, R. Grandin, E. Pathier, and V. Pinel (2011), Presentation of the small baseline NSBAS Processing chain on a case example : The etna deformation monitoring from 2003 to 2010 using Envisat data., *Proc. ESA Fringe*.

Doin, M.-P., C. Twardzik, G. Ducret, C. Lasserre, S. Guillaso, and S. Jianbao (2015), InSAR measurement of the deformation around Siling Co Lake: Inferences on the lower crust viscosity in central Tibet, *J. Geophys. Res.: Solid Earth*, *120*(7), 5290–5310.

Ducret, G., M.-P. Doin, R. Grandin, C. Lasserre, and S. Guillaso (2014), DEM corrections before Unwrapping in a Small Baseline Strategy for InSAR Time Series Analysis, *Geoscience and Remote Sensing Letters, IEEE*, *11*, 696–700.

Grandin, R., M.-P. Doin, L. Bollinger, B. Pinel-Puysségur, G. Ducret, R. Jolivet, and S. N. Sapkota (2012), Long-term growth of the Himalaya inferred from interseismic InSAR measurement, *Geology*, *40*(12), 1059–1062.

Jolivet, R., R. Grandin, C. Lasserre, M.-P. Doin, and G. Peltzer (2011), Systematic InSAR tropospheric phase delay corrections from global meteorological reanalysis data, *Geophys. Res. Lett.*, *38*(17).

Jolivet, R., P. S. Agram, N. Y. Lin, M. Simons, M.-P. Doin, G. Peltzer, and Z. Li (2014), Improving InSAR geodesy using global atmospheric models, *Journal of Geophysical Research: Solid Earth*, *119*(3), 2324–2341.

Leppäranta, M. (1993), A review of analytical models of sea-ice growth, *Atmosphere-Ocean*, *31*(1), 123–138.

López-Quiroz, P., M.-P. Doin, F. Tupin, P. Briole, and J.-M. Nicolas (2009), Time series analysis of Mexico City subsidence constrained by radar interferometry, *J. Applied Geophysics*, *69*(1), 1–15.

Pan, G.-t., J. Ding, D.-s. Yao, and L.-q. Wang (2004), Geological map of the Qinghai-Xizang (Tibet) Plateau and adjacent areas, *Chengdu Cartographic Publishing House*.

Pinel, V., A. Hooper, D. la Cruz-Reyna, G. Reyes-Davila, M. Doin, et al. (2008), Study of the deformation field of two active mexican stratovolcanoes (popocatepelt and colima volcano) by time series of InSAR data.

Pinel-Puyssegur, B., R. Michel, and J.-P. Avouac (2012), Multi-Link InSAR Time Series: Enhancement of a Wrapped Interferometric Database, *IEEE J. Selected Topics in Applied Earth Observations and Remote Sensing*, *5*(3), 784–794.

Rosen, P. A., S. Hensley, G. Peltzer, and M. Simons (2004), Updated repeat orbit interferometry package released, *Eos, Transactions American Geophysical Union*, *85*(5), 47–47.

Stefan, J. (1891), Über die theorie der eisbildung, insbesondere über die eisbildung im polarmeere, *Annalen der Physik*, *278*(2), 269–286.

Strozzi, T., and U. Wegmuller (1999), Land subsidence in mexico city mapped by ERS differential sar interferometry, in *Geoscience and Remote Sensing Symposium, 1999. IGARSS'99 Proceedings. IEEE 1999 International*, vol. 4, pp. 1940–1942, IEEE.

Yun, S.-H., H. Zebker, P. Segall, A. Hooper, and M. Poland (2007), Interferogram formation in the presence of complex and large deformation, *Geophysical Research Letters*, *34*(12).